

Optimized algebraic reconstruction technique for generation of grain maps based on three-dimensional x-ray diffraction (3DXRD)

Xiaowei Fu

Erik Knudsen

Henning F. Poulsen

Risø National Laboratory

Materials Research Department

DK-4000 Roskilde, Denmark

E-mail: henning.friis.poulsen@risoe.dk

Gabor T. Herman

City University of New York

Graduate Center

Computer Science Department

New York, New York 10016

Bruno M. Carvalho

Stevens Institute of Technology

Computer Science Department

Hoboken, New Jersey 07030

Hstau Y. Liao

City University of New York

Graduate Center

Computer Science Department

New York, New York 10016

1 Introduction

Mapping the grain structure is a vital part of most materials studies of polycrystals or powders. Until recently, for monophase materials, maps could be provided only by optical or electron microscopy on surfaces. The generation of three-dimensional (3D) maps required serial sectioning. Sectioning is a tedious procedure, which furthermore, and very importantly, also is incompatible with dynamic studies because of its destructive nature.

Recently, two synchrotron-based x-ray diffraction methods have been introduced as tools for 3D structural characterization of polycrystals. The first is a scanning approach where the sample is translated with respect to a polychromatic microbeam.¹ Submicron resolution can be obtained in this way, but the method is inherently slow due to the scanning procedure. The second method is Three-Dimensional X-Ray Diffraction (3DXRD) microscopy,²⁻⁵ where a monochromatic beam is used. With 3DXRD, the aim is to characterize a whole layer in the sample simultaneously, thereby increasing the data acquisition rate and enabling dynamic studies.

3DXRD is based on diffraction with very penetrating high-energetic ($E \geq 50$ keV) x-rays⁶ such that the properties of the individual grains can be characterized within

Abstract. Recently, an algebraic reconstruction method has been presented for generation of three-dimensional (3D) maps of the grain boundaries within polycrystals. The grains are mapped layer by layer in a nondestructive way by diffraction with hard x rays. We optimize the algorithm by means of simulations and discuss ways to automate the analysis. The use of generalized Kaiser-Bessel functions as basis functions is shown to be superior to a conventional discretization in terms of square pixels. The algorithm is reformulated as a block-iterative method in order to incorporate the instrumental point-spread function and, at the same time, to avoid the need to store the set of equations. The first reconstruction of a full layer and two neighboring 3D grains from experimental data are demonstrated. © 2006 Society of Photo-Optical Instrumentation Engineers. [DOI: 10.1117/1.2390680]

Subject terms: x-rays; diffraction; three dimensions; mapping; tomography; synchrotron radiation.

Paper 050872R received Nov. 1, 2005; revised manuscript received Mar. 31, 2006; accepted for publication Apr. 6, 2006; published online Nov. 29, 2006. This paper is a revision of a paper presented at the SPIE conference on Developments in X-Ray Tomography IV, Aug. 2004, Denver, Colorado. The paper presented there appears unrefereed in SPIE proceedings Vol. 5535.

millimeter-to-centimeter thick specimens. Diffraction spots are acquired with a virtual 3D detector, while rotating the sample around one axis. The spots are sorted with respect to grain of origin by an indexing algorithm, GRAINDEX.³ Simultaneously, the position, volume, elastic strain tensor, and crystallographic orientation are determined.⁴ Under favorable conditions, the dynamics of several hundred embedded grains can be followed during *in situ* deformation^{7,8} or annealing experiments.^{9,10} The method has been implemented for a dedicated instrument—the 3DXRD microscope—at beamline ID11 at the European Synchrotron Radiation Facility (ESRF).⁵

Notably, 3DXRD can also be used to generate 3D maps of the grain boundaries^{2,4,5} and even to produce movies of the morphology changes of embedded grains during annealing events such as recrystallization.¹¹ To generate the grain maps, our group at Risø has suggested a number of numerical approaches, ranging from a simple back projection of diffraction spots⁴ to transform methods¹² and algebraic methods.^{2,13} In the latter methods, the problem is cast in terms of an “inverse problem.” Solutions to such problems—reconstructions—have been investigated in great detail, driven by applications in imaging such as computed tomography (CT).¹⁴⁻¹⁶ More specifically, the 3DXRD-based transform and algebraic methods are deriva-

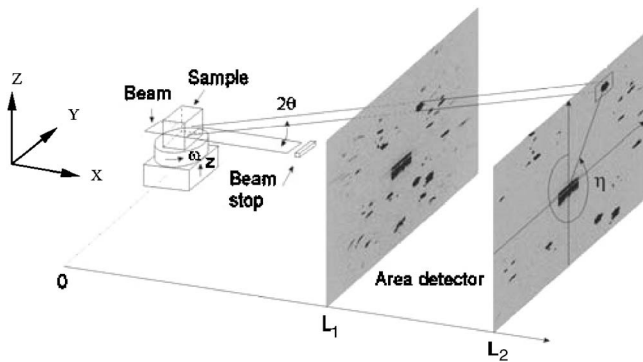


Fig. 1 Sketch of the experimental geometry. Spots arising from the same reflection (and the same grain) at different sample-detector distances are identified. The angles 2θ , η , and ω as well as the axes (x , y , z) of the laboratory coordinate system are defined.

tives of the well-known filtered back projection (FBP)^{15–17} and algebraic reconstruction technique (ART)^{14,15,18} routines, respectively.

Three conclusions emerge from the work on 3DXRD reconstructions. First, one can impose conditions that vastly simplify the geometry. Examples of such conditions are nonoverlapping diffraction spots—in which case, the grains can be reconstructed independently—and grains with a negligible mosaic spread. Second, CT and 3DXRD, reconstructions are inherently different. For instance, with 3DXRD, an additional symmetry is introduced by the crystallography of the material. This implies that the number of projections cannot be determined at will, as it can in CT. Third, in general, algebraic methods are superior.¹⁹ Full use can be made of simplification in geometry or additional constraints. Furthermore, such algorithms can be extended to handle combined diffraction and absorption contrast tomography data.

In this paper, we concentrate on the simplest geometry: that of “perfect” grains (negligible mosaic spread) being illuminated by a line-focused beam while giving rise to mainly nonoverlapping diffraction spots. For a large fraction of materials, experiments can be tailored to fulfill this condition. We start by summarizing from our previous work² the ART variant relevant to this geometry—2D-ART. Next, four details of the analysis are discussed, and the algorithm is optimized by means of simulations. The suggested improvements are in part inspired by work on algebraic reconstruction methods in other fields.^{20,21} Last, the first reconstructed layer based on experimental data is presented.

2 Summary of 2D-ART

The geometry underlying the 3DXRD method is described in detail in our previous works.^{2,5} A sketch is provided in Fig. 1. A beam of monochromatic hard x rays is focused in one direction to illuminate a layer in the sample. The sample is mounted on an ω rotation stage, with the rotation axis perpendicular to the beam. Some of the grains will give rise to diffracted beams, which are transmitted through the sample to be observed as spots by a flat two-dimensional (2D) detector. The detector exhibits a high spatial resolution and is positioned at a small sample-

detector distance L_1 . It is aligned perpendicular to the monochromatic beam. Acquisitions are made at a set of equiangular ω -settings in steps of $\Delta\omega$. During each exposure, the sample is oscillated by $\pm\Delta\omega/2$ in order to sample the diffracted intensity uniformly. As an option, the whole procedure may be repeated one or more times at larger sample-detector distances, L_2, \dots, L_n . The data obtained at the larger distances are used only for GRAINDEX, not for the reconstruction part.

We proceed to derive an algebraic approach to the reconstruction of the in-plane shape of a single grain. Based on the output from GRAINDEX, grains can be reconstructed separately, and layer by layer. Hence, it suffices to derive a formalism for the generation of the in-plane shape of one grain.

In the version of 2D-ART presented earlier,² the illuminated plane in the sample is tessellated into a set of squares (pixels) on a regular 2D grid. The aim of the reconstruction is to determine the density x_j of these pixels. For pixels fully outside the grain, the density should be zero, and for pixels fully inside, it should be equal to a materials’ constant ρ_0 . Pixels at the boundary may be partly inside the grain and should therefore have intermediate values.

For each of the diffraction spots associated with the grain of interest, an area-of-interest (AOI) on the detector is identified. The AOI is centered on the projected center of mass (CMS) of the grain. The background-corrected pixel intensities within the AOI are normalized by the structure factor and the Lorentz factor²² for the reflection. For each reflection r , the normalized intensities are saved in an array b^r . It is essential that the complete integrated intensity of each diffraction spot is included in the analysis. Any overlapping spots or diffraction spots that are split over several ω -settings (due to a minor mosaic spread) therefore have to be excluded from the analysis.

Central to the method is the assumption of kinematical scattering.²² This enables a formulation in terms of a set of linear equations. For each reflection r ,

$$A^r x = b^r. \quad (1)$$

Here the unknown x comprises the pixel densities, and the information on the experimental setup and diffraction geometry is stored in A^r .

Next the A^r s for the reflections are piled into a block matrix A , and the compound array b is defined:

$$A = \begin{pmatrix} A^1 \\ A^2 \\ \vdots \end{pmatrix}; \quad b = \begin{pmatrix} b^1 \\ b^2 \\ \vdots \end{pmatrix}. \quad (2)$$

With these definitions, the basic equation for the reconstruction of the shape of the grain is

$$\sum_{j=1}^N A_{ij} x_j = b_i; \quad i = 1, \dots, M. \quad (3)$$

The solution is constrained by the requirement stated here—namely, for all j ,

$$0 \leq x_j \leq \rho_0. \quad (4)$$

A full grain map can be obtained by superposing the solutions—the shapes—of the individual grains. However, such a map will not be space filling, as boundaries from neighboring grains may overlap or leave “voids” in the map. These so-called ambiguous areas are located as rims in the proximity of the grain boundaries. To avoid this problem and produce space-filling maps, there are two options. The straightforward approach is to allocate each pixel in the ambiguous area to a neighboring grain according to which single-grain reconstruction resulted in the largest density at that pixel. The better, but more time-demanding, method is to extend the ART method to simultaneous reconstruction of neighboring grains.² Let us start by two such grains, symbolized by 1 and 2. Let $A_1x_1=b_1$ and $A_2x_2=b_2$ be the one-grain equations as defined earlier, with x_1 and x_2 referring to the same pixels. Then we define the compound system

$$A = \begin{pmatrix} A_1 & 0 \\ 0 & A_2 \end{pmatrix}; \quad b = \begin{pmatrix} b_1 \\ b_2 \end{pmatrix}; \quad x = \begin{pmatrix} x_1 \\ x_2 \end{pmatrix}. \quad (5)$$

With these definitions, Eq. (3) applies again. In the vicinity of the boundary between the two grains, the constraint of Eq. (4) becomes

$$0 \leq x_{1i} \leq \rho_0; \quad 0 \leq x_{2i} \leq \rho_0; \quad x_{1i} + x_{2i} = \rho_0; \quad \forall i. \quad (6)$$

Generalization to more neighbors is straightforward. Four is sufficient, as a maximum of four grains can be adjacent to each other in one layer, cf. the four-color problem in mathematics. (This generalization of the algorithm to several grains is outside the scope of this paper.)

2.1 The ART Algorithm

ART is a simple iterative routine, an adaptation of the Kaczmarz algorithm.²³ Solutions x^{k+1} are found by progressively projecting the previous solutions x^k on the hyperplane represented by the $i(k)$ 'th equation [mathematically, $i(k)=k(\text{mod } M)+1$]:

$$\underline{x}^{k+1} = \underline{x}^k + \lambda \left(\frac{b_{i(k)} - \sum_{j=1}^N A_{i(k)j} x_j^k}{\sum_{j=1}^N A_{i(k)j}^2} \right) \underline{a}_{i(k)}, \quad (7)$$

with $\underline{a}_{i(k)} = (A_{i(k)1}, \dots, A_{i(k)N})^T$. The bracketed term is a scalar, representing a normalized difference between the measured intensity in the pixel with index $i(k)$, $b_{i(k)}$, and the simulated intensity in that pixel given the estimate x^k . This algorithm is known to converge to the minimum-norm solution for a consistent system of equations.^{23,24} In the case of an inconsistent system, the sequence of x^k will oscillate around the least-squares solution.

As an important practical consideration, we note that for each iterative step in ART, only a single row, $A_{i(k)j}$; $j = 1, \dots, N$, is needed. Thus, instead of evaluating the entire matrix prior to the iterative procedure, we can calculate each row as ART needs it. The memory requirement with respect to A in such an implementation of ART does not scale with the number of reflections, enabling the use of

many, if available, reflections to ensure reconstruction quality. On the other hand, this saving is bought with processing time, since each row is now evaluated anew for $k > M$. Empirically, we find the cost of multiple evaluations of each row in A to be moderate, as the number of cycles through the data that are necessary to obtain good reconstructions is usually less than fifteen.

To improve the rate of convergence, the order of the rows i in Eq. (7) are permuted randomly so that consecutive hyperplanes are likely to be nearly orthogonal to each other.² The so-called relaxation parameter, $0 < \lambda < 1$, is introduced because it improves initial convergence. The starting estimate x^0 is set to an array of zeros.

For the single-grain reconstruction, two restrictions are applied after each step:

1. Fully constrained: x^k is set to $\min[\rho_0, \max(0, x^k)]$.
2. Compact support: $x_j^k = 0$ if the projection of the j 'th pixel is outside any of the AOIs.

The application of restriction 1 reduces the “salt-and-pepper” noise substantially.² It is crucial when dealing with only a few reflections.¹³

The ART step of Eq. (7) is repeated until convergence is obtained. To characterize convergence, the normalized 1-norm is used as a figure-of-merit function, $FOM1$:

$$FOM1 = \frac{\|A\underline{x} - \underline{b}\|_1}{\|\underline{b}\|_1}. \quad (8)$$

Evidently, $FOM1=1$ for x^0 and $FOM1 \rightarrow 0$ for ideal solutions.

Once a solution is found, it is “binarized” by using a threshold: a pixel with index j is defined as belonging to the grain if and only if $x_j > \rho_0/2$. For the simultaneous reconstruction of neighboring grains, the constraint on density and the binarization are implemented in similar ways.

3 Optimization

As noted, the number of projections with 3DXRD cannot be chosen arbitrarily, and therefore the resolution of reconstructions cannot be improved by simply decreasing $\Delta\omega$. Also, to take full advantage of 3DXRD's potential for dynamic and/or *in situ* measurements, it is vital to shorten data acquisition times as well as computing times. Hence, it is important to optimize the 3DXRD ART algorithms, without sacrificing reconstruction quality. We show results along several lines of optimization, which presently have yet to be combined. First, two measures of reconstruction quality, figure-of-merit functions, are introduced, and thereafter, some optimization steps are discussed in more detail.

To measure the deviation between the original and the reconstructed images, the relative number of incorrectly assigned voxels is used. The resulting figure-of-merit functions are defined as

$$FOM2 = \frac{\|\underline{x}^{orig,bin} - \underline{x}^{sol,bin}\|_1}{\|\underline{x}^{orig,bin}\|_1}, \quad (9)$$

in terms of the binarized grain map, and

$$FOM3 = \frac{\|\underline{x}^{orig} - \underline{x}^{sol}\|_1}{\|\underline{x}^{orig}\|_1}, \quad (10)$$

in terms of the “true” density map.

3.1 Choice of Reflections

As noted, diffraction spots are assumed to be distinct, facilitating independent reconstruction of each grain. Keeping this in mind, overlapping spots should be excluded from the reconstruction. GRAINDEX excludes overlapping spots to an extent, yet reconstruction attempts indicate that a further screening of diffraction spots is needed to achieve high-quality reconstructions by ART. Given the relatively small number (that is, when compared¹⁴ to CT) of projections available to the algorithm, a single diffraction spot with a high degree of experimental error may substantially lower the reconstruction quality.

Several schemes for weeding out diffraction spots have been identified and implemented:

- Sort spots according to an intensity measure defined as the integrated intensity normalized by the Lorentz and structure factors.²² Exclude those above an upper threshold (indicating a probable double spot) or below a lower threshold (indicating a not fully illuminated spot). Similar types of filtering are used routinely in single-crystal crystallography.
- Simulate spots and exclude spots deviating significantly from their simulated CMS coordinates.
- Evaluate the shape of the spots, removing spots that do not, after transform, conform to the mean shape. Notice that a scheme of this type has the drawback that it scales badly with the number of reflections.

None of these schemes have proven sufficiently reliable on their own. Therefore, two or more should be used in conjunction. If after weeding a sufficient number of reflections remain (≥ 5), reconstructions of reasonable quality are attainable.

We mention that weeding out erroneous reflections further reduces the already limited number of usable reflections, rendering all the information contained in the bad spots unusable. It may be better to assign instead a relative

weight to each reflection spot and, correspondingly, let the relaxation parameter in Eq. (7) be a function of the reflection number r . This procedure still requires a quantitative measure of spot quality, but it also requires an additional step to correlate the quality measure with the relaxation parameter.

3.2 Blobs

The choice of basis functions has been discussed in depth in the literature on inverse problems. Lewitt²⁰ lists the following set of desirable properties:

- The basis functions should be localized in space.
- The Fourier transforms (FT) of the basis functions should be effectively localized around the origin.
- The basis functions (and their FT) should have rotational symmetry in n dimensions.
- Convenient formulas should be available for the calculation in n dimensions of the FT, the k -plane Radon transform, and the gradient of the basis functions.
- The basis functions should be differentiable a desired number of times.

The full argumentation behind this set is beyond the scope of this article. However, two points should be emphasized. First, the rotational symmetry is important because it facilitates the use of a lookup table. Second, the fact that the basis functions are nearly band-limited automatically removes “salt-and-pepper” noise, which is otherwise typically removed in an *ad hoc* manner by smoothing (with a loss of resolution as result).

It is clear that the conventional square pixels (in 2D), or the cube-shaped voxels (in 3D), do not fulfill any of the requirements listed except the first one. As an alternative conforming to the list of requirements, Lewitt suggests the use of generalized (or modified) Kaiser-Bessel window functions,²⁰ generally known as “blobs.” In this case, the image is represented by the superposition of overlapping blobs whose centers are arranged on a regular grid in the image space. Unlike a voxel, a blob has a bell-shaped profile that gives a smooth transition in the radial direction from a high value at the center of its supporting sphere to value zero at the surface of that sphere.²⁵ Blobs are defined by:

$$b_{m,\alpha,a}(r) = \begin{cases} \frac{I_m \left\{ \alpha \left[1 - \left(\frac{r}{a} \right)^2 \right]^{1/2} \right\} \left\{ \left[1 - \left(\frac{r}{a} \right)^2 \right]^{1/2} \right\}^m}{I_m(\alpha)}, & \text{if } 0 \leq r \leq a, \\ 0, & \text{otherwise.} \end{cases} \quad (11)$$

Here r is the radial distance from the blob center. The blob is defined by three parameters: the order m of the modified Bessel function I_m , the radius a that determines the blob size, and the so-called taper-parameter α , which controls the blob shape.

Blobs have been demonstrated to be more efficacious than voxels in applications in electron microscopy (EM)²⁶ and positron emission tomography (PET).²⁷ Inspired by this success, the concept of blobs is introduced into 3DXRD reconstructions by 2D-ART.

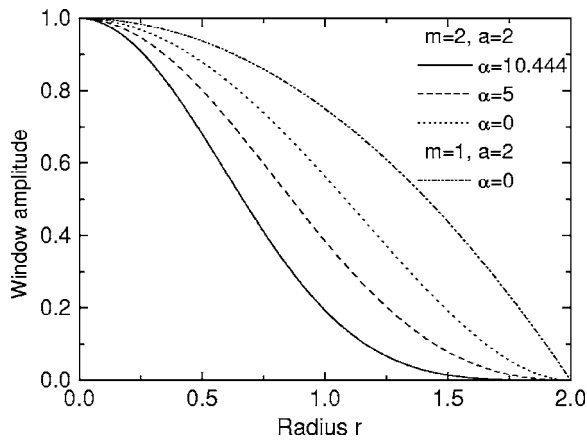


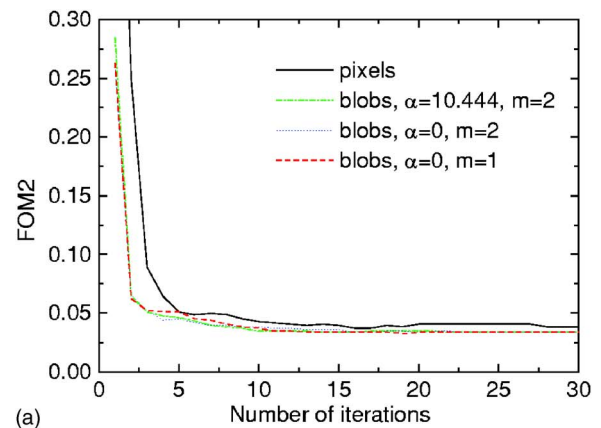
Fig. 2 Examples of the modified Kaiser-Bessel window functions as a function of parameters m and α .

First we discuss the selection of the three parameters: m (a non-negative integer) and a and α (non-negative real numbers). The parameter m may in principle be chosen arbitrarily, but in practice, m must be at least 2 to get a “smooth” blob and is further limited by the undesirable consequences²⁸ of the extra smoothness provided by larger values of m . Therefore, in this paper, m is set to 2. As to the other parameters, researchers in PET selected the body-centered cubic (BCC) grid, and α was then optimized accordingly.²⁵ Since a different algorithm is developed based on the 3DXRD geometry, these parameters have been reevaluated in this paper. To compare the result with ART-pixel, in this paper, the grid type and grid size are fixed as that in ART-pixel. A few blob shapes as a function of the parameters discussed here are shown in Fig. 2.

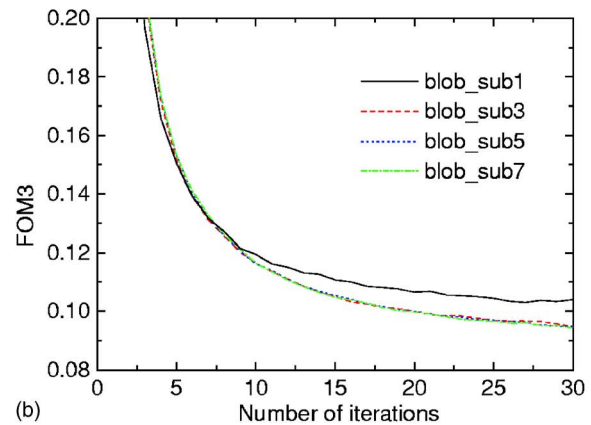
For the 3DXRD implementation of 2D-ART, blobs were placed on a square grid according to the estimated size of the grain, and each grid was subdivided into $q \times q$ subpixels for varying q . The values of the Kaiser-Bessel functions were precalculated and were tabulated to avoid unnecessary computations. Each subpixel within each single blob was given a value by accessing the table. The contribution from this subpixel to a pixel on the detector was simulated in the same way as for a pixel-based implementation. Due to the specific geometry of 3DXRD, unlike the blob-based algorithm used in PET or EM reconstruction,^{26,27} no line integrals were calculated in the 3DXRD reconstruction. Once the weights assigned to each of the blobs have been obtained, a “blob-driven” approach performs the conversion from the blob domain to the pixel domain. In this approach, for every blob, a value for each pixel that intersects it is computed, and these values are accumulated in the pixel domain.

For comparison, 2D-ART simulations were performed with both pixels and blobs. Parameters were identical to those in our previous work² except for a grid size of $1.15 \times 1.15 \mu\text{m}$. In the following, we report on our initial results for a single grain section. For this grain, five reflections were available.

$FOM2$ is plotted in Fig. 3(a) as a function of number of iterations for pixels and three different types of blobs. In all cases, a subdivision of each grid into 7×7 subpixels was used. As can be seen in the figure, $FOM2$ initially drops



(a)



(b)

Fig. 3 The influence of blob-shape parameters on the figure-of-merit functions $FOM2$ and $FOM3$, as defined in Eqs. (9) and (10), respectively. (a) $FOM2$ as a function of number of iterations, pixels versus various blobs. (b) $FOM3$ as a function of number of iterations, showing the effects of varying the number of subdivisions of the same blob, where blob_sub q denotes a $q \times q$ subdivision.

when blobs are introduced, but there is no discernible difference between the three types of blob. Above five iterations, both the blob and the pixel version saturate, the pixel version at a slightly higher value. We add that the differences between pixel- and blob-based simulations are substantially bigger when the number of reflections is reduced. Similar results are obtained using $FOM3$ as the measure of convergence.

In terms of the density maps, it can be seen clearly in Figs. 4(a)–4(d) that the reconstructed grain maps obtained by ART-blobs are more homogeneous than those obtained by ART-pixels.

As the degree of subdivision may have a significant impact on the efficiency of the procedure, it is an important parameter to evaluate. In Fig. 3(b), $FOM3$ is plotted for blobs with subdivisions of 1×1 , 3×3 , 5×5 , and 7×7 . Evidently, a subdivision of 3×3 is sufficient. Similar results were obtained using $FOM2$.

In summary, results from both Figs. 3 and 4 demonstrate that reconstruction using blobs is superior to that using pixels. Even if each grid is subdivided into only 3×3 , a reasonably good resolution can still be achieved without losing reconstruction speed. The results are seemingly robust with respect to the choice of the parameters characterizing the

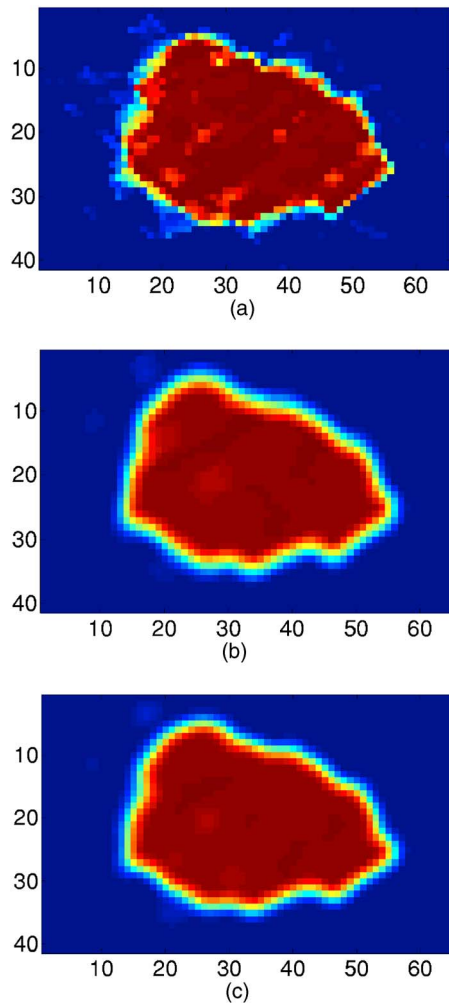


Fig. 4 Reconstructed density maps for simulated data representing one grain. Parameters related to blob shape and number of subdivisions are varied. The (x, y) coordinate system is shown in units of μm . In all cases: radius of blob=2, number of reflections=5, number of iterations=30. (a) Pixels, subdivision=7; (b) blobs, $m=2$, $\alpha=10.444$, subdivision=1; (c) blobs, $m=1$, $\alpha=0$, subdivision=7; (d) blobs, $m=2$, $\alpha=0$, subdivision=7.

blob. Varying parameters of blob shape does not influence the resolution (*FOM2* and *FOM3*) dramatically. This is in contrast to findings elsewhere that the optimization of blob parameters is very important.²⁸

3.3 Block-Iteration and Point-Spread Function

An important alternative approach to ART as described in Sec. 2.1 is to use a block-iterative version of it.²¹ In such a version, instead of considering the individual rows of Eq. (3) one by one, we consider each partial problem, $A^r \underline{x} = \underline{b}^r$, in turn, for each reflection r . Such an approach is sometimes preferable, mainly for instrumental, but also for numerical, reasons.²¹ This concept enables us to correct for the point-spread function (psf) of the detector in use in experiments (Sec. 4) and for nonideal x-ray beam profiles, while keeping the problem numerically practical.

In practice, the x-ray beam has finite thickness and an anisotropic beam profile. This may be modeled by extending sample plane pixels to voxels mimicking the beam pro-

file and projecting these voxels onto the detector plane. In combination with the psf, this associates a “footprint” with each sample plane pixel.

We incorporate these effects into ART as a correction matrix G , which is multiplied with the weight matrix before reconstruction. The elements in G are given by the psf convolved with the projection of the voxel.

It may be noted that these corrections were included in our reconstructions on experimental data (Sec. 4), where reconstruction quality was found to be poor without correction.

3.4 Discretization

As noted, the construction of the A^r matrices should reflect the geometry of the experimental setup as well as the diffraction geometry. This may be done by the following procedure. First, check whether the center of a given voxel, projected in the direction associated with reflection r , falls inside the associated detector AOI. If so, the voxel is subdivided into subvoxels, and then the element in A^r is the ratio between the number of subvoxel centers that project into the AOI and the total number of subvoxels within the voxel.

A less expansive algorithm has been devised, weighing the voxel projection with the length of a line segment through the voxel in the diffraction direction. To investigate this further, we have reconstructed a grain from simulated data using the two weighing schemes. With all other parameters equal, the faster line approximation yields somewhat noisier reconstructions [Fig. 5(b)]. After binarization, however, no significant difference in reconstruction quality is apparent [Fig. 5(a)], in which case, the faster algorithm may be used, for instance, for mapping purposes.

4 Experimental Data

The experimental verification was performed on a well-annealed aluminum polycrystal with an average 3D grain size of $150 \mu\text{m}$. A cylindrical specimen was used with a height of 3 mm and a radius of 0.4 mm. The experiment was performed at the 3DXRD microscope at ESRF. A monochromatic beam of 50 keV was focused to an elongated spot of $2 \times 1,000 \mu\text{m}^2$. This spot illuminated a layer near the center of the specimen, which was mounted with the cylindrical axis parallel to the ω axis. Images were acquired over an ω range of 90 deg, in steps of $\Delta\omega=1$ deg. The 2D detector was a 1,536-by-1,024-pixel CCD camera with a resolution of $2.3 \times 2.3 \mu\text{m}^2$. Three detector positions were used with distances of 4.2, 5.7, and 7.2 mm to the sample, respectively. Thirty-six layers in the sample with an interval of $5 \mu\text{m}$ were measured. In total, $\sim 10,000$ images were recorded. Results for some layers near the center of the sample will be reported later.

Before inputting information regarding the spots into ART, a sequence of preprocessing steps were performed:

1. Correcting for the spatial distortion and flat-field effects of the data recorded on the detector for each sample layer of interest by FIT2D software.²⁹ The image background was also subtracted.
2. Sorting of all the reflections and finding grains as well as their orientations (Euler angles) by the GRAINDEX program.

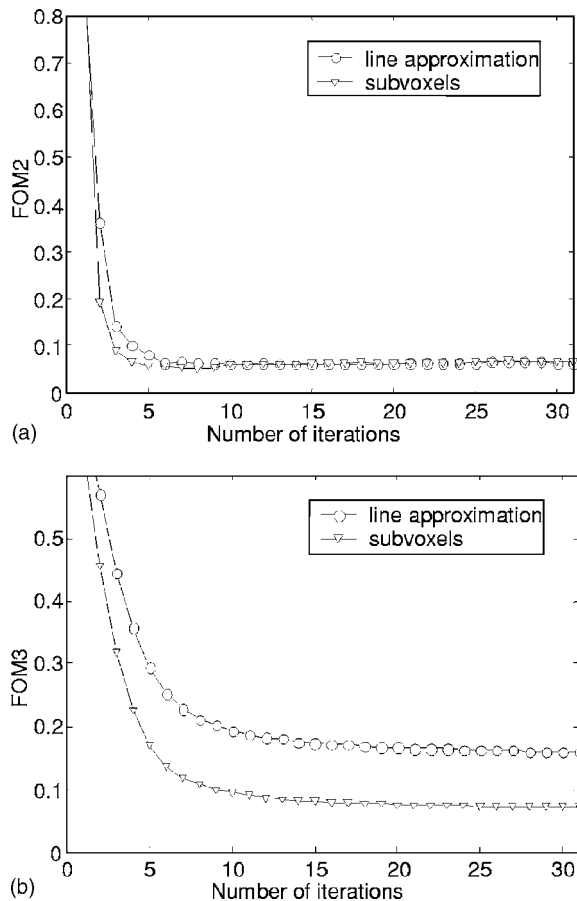


Fig. 5 Figure-of-merit functions $FOM2$ and $FOM3$ as defined by Eqs. (9) and (10), for reconstructions using two different weighting schemes. The subvoxel scheme, denoted by triangles, exhibits better convergence than the line-segment approximation scheme, denoted by circles, for true density maps (b), but after binarization, the quality of reconstruction is almost equal in both cases (a). Eight simulated reflections were used for reconstruction.

3. Deleting both overlapped and faint spots from the database.
4. Nonlinear least-squares fitting of experimental and geometric parameters to minimize system errors, followed by estimating position and orientation parameters by a global fit.

The result for the independent reconstruction of 27 grains based on five reflections and normally four diffraction families: $\{111\}$, $\{200\}$, $\{220\}$, and $\{311\}$ are shown in Fig. 6. The standard deviation between simulated and observed spot positions varied between 0.9 and $2.4 \mu\text{m}$ for these grains. With a reconstructed pixel size of $2.3 \mu\text{m}$, the matrix \mathbf{A} was typically nearly square with a size around $2,500 \times 2,500$. The relaxation parameter λ was set to 0.1 .

The $FOM1$ s were in the range 0.15 to 0.24 , with the scatter mainly reflecting the size of the AOI used. From the overlap between grains and voids in Fig. 6, we estimated the spatial resolution to be $\sim 5 \mu\text{m}$. The main limitation is identified to be the instrumental psf. A few grains are obviously missing from the map—for the particular geometry used, the number of independent reflections were too few to enable reconstruction.

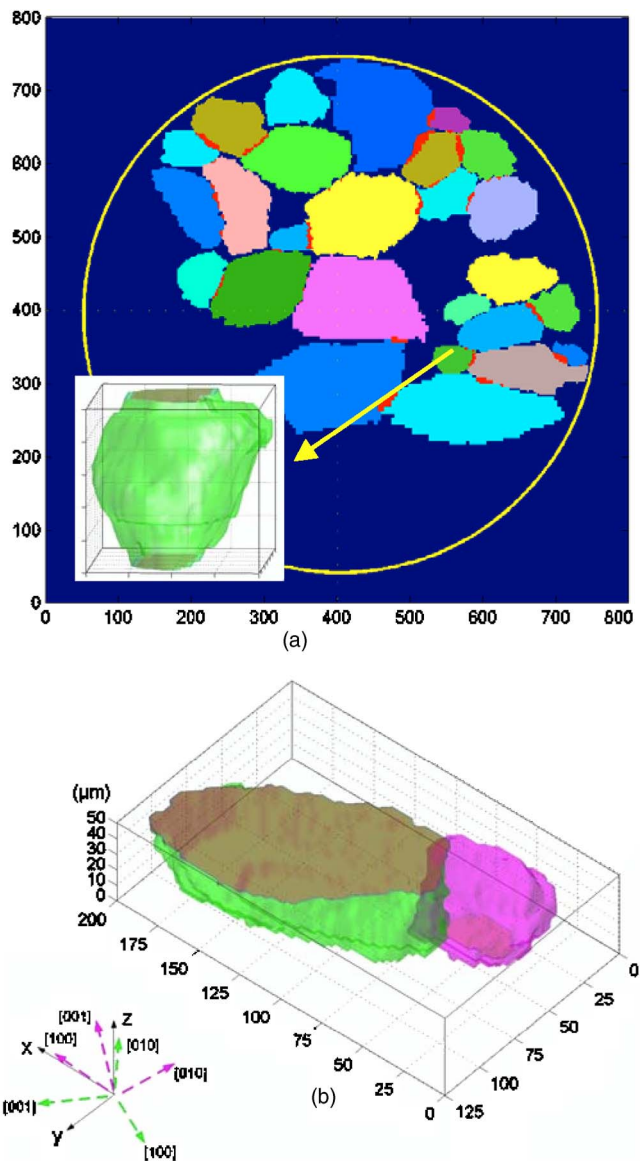


Fig. 6 Partial grain map of one embedded layer within an Al polycrystal in units of μm . The grain sections were reconstructed independently. The colors represent the orientations of the grains. The solid yellow circle indicates the surface of the polycrystal. Regions of overlap between the grain sections are marked in red. This data set was acquired in 10 min. By stacking layers, 3D maps are obtained; an example is shown in the insert (Color online only).

Three-dimensional maps of selected grains are generated by stacking the layers serially with the interval of $5 \mu\text{m}$ (Fig. 6). Interpolations such as nearest-neighbor interpolation are used to fill in the spacing between. The crystallographic axes of two neighboring grains are also shown in the Fig. 6(b). The grain seen to the left in Fig. 6(b) is very large, and only the bottom section shares a grain boundary with the grain seen to the right. Therefore, only this bottom section of the big grain is shown in Fig. 6(b) (and one gets the impression of looking inside the big grain).

In the present work, the resolution in the vertical direction (z axis) is in the range of 1 to $5 \mu\text{m}$. This resolution is determined by the height of the x-ray beam in the z direc-

tion (here, $2\ \mu\text{m}$ was chosen), the intervals of the measure, and the algorithm for interpolation. Some algorithms based on the so-called shape-based interpolation⁵⁰ between the slices that is used in CT reconstruction are being investigated. The precise contour of both the top and bottom sections of the selected grains could not be fully reconstructed due to the lack of information. Measuring more layers could easily solve this problem.³¹

5 Discussion

Several computational “tricks” may be employed to increase the efficiency of the ART procedure. First, by identifying AOIs of minimal size and by restraining the reconstruction to include a minimum of zero elements surrounding the local representation of each grain, a significant reduction in running time may be achieved. Second, reorganizing matrix rows and/or reflections in a more elaborate but more efficient scheme is of comparatively low cost, which may reduce the number of iterations—yielding a net reduction in running time. Third, further optimization in evaluating the matrices A' is feasible, for example, by limiting the use of trigonometric functions to a minimum. Finally, one can take advantage of parallel computing, in conjunction with the block-iterative version²¹ of Eq. (7); this will yield faster performance, particularly for large reconstructions.

6 Conclusions

The 2D-ART method is shown to be able to provide high-quality maps of grain boundaries within polycrystals. The algorithm-related parameters have been optimized and the method automated, enabling a fast and robust data analysis.

It is believed that data acquired here by 3DXRD and ART image reconstruction may be of significant importance for research in materials science. The data contain full information about the crystallographic orientation and the morphology of each individual grain; they are 3D and non-destructive. Moreover, direct information is thus obtained about the crystallographic misorientation across grain boundaries, and the boundary plane is known for each point on the grain boundary, which could not be obtained by other techniques. These parameters are essential in understanding the motion of the grain boundary and many materials properties and phenomena in materials science.

Acknowledgments

Discussions with S. Schmidt, E. M. Lauridsen, and T. Markussen are much appreciated. L. Margulies, S. F. Nielsen, and A. Terry are acknowledged for participating in the synchrotron experiment and P. B. Olesen for sample preparation. ESRF is acknowledged for provision of beam time. This work was supported by the Danish National Research Foundation through the Center for Fundamental Research: Metal Structures in Four Dimensions and by the Danish Natural Science Research Council via Dansync. The research contributions to this paper of Gabor T. Herman, Bruno M. Carvalho, and Hstau Y. Liao were supported by NIH Grant No. HL70472 and NSF Grant No. DMS0306125.

References

1. B. C. Larson, W. Yang, G. E. Ice, J. D. Budai, and T. Z. Tischler, “Three-dimensional x-ray structural microscopy with submicrometre resolution,” *Nature (London)* **415**, 887–890 (2002).
2. H. F. Poulsen and X. Fu, “Generation of grain maps by an algebraic reconstruction technique,” *J. Appl. Crystallogr.* **36**, 1062–1068 (2003).
3. E. M. Lauridsen, S. Schmidt, H. F. Poulsen, and R. M. Suter, “Tracking: a method for structural characterization of grains in powders or polycrystals,” *J. Appl. Crystallogr.* **34**, 744–750 (2001).
4. H. F. Poulsen, S. F. Nielsen, E. M. Lauridsen, S. Schmidt, R. M. Suter, U. Lienert, L. Margulies, T. Lorentzen, and D. Juul Jensen, “Three-dimensional maps of grain boundaries and the stress state of individual grains in polycrystals and powders,” *J. Appl. Crystallogr.* **34**(6), 751–756 (2001).
5. H. F. Poulsen, *Three-Dimensional X-ray Diffraction Microscopy, Springer Tracts in Modern Physics 205*, Springer Verlag, Berlin (2004).
6. R. Bouchard, D. Hupfeld, T. Lippmann, J. Neufeind, H.-B. Neumann, H. F. Poulsen, U. Rütt, T. Schmidt, J. R. Schneider, and M. von Zimmermann, “A triple-crystal diffractometer for high-energy synchrotron radiation at the HASYLAB high-field wiggler beamline BW5,” *J. Synchrotron Radiat.* **5**, 90–101 (1998).
7. L. Margulies, G. Winther, and H. F. Poulsen, “In situ measurement of grain rotation during deformation of polycrystals,” *Science* **291**, 2392–2394 (2001).
8. H. F. Poulsen, L. Margulies, S. Schmidt, and G. Winther, “Lattice rotations of individual bulk grains: part I: 3D x-ray characterization,” *Acta Mater.* **51**, 3821–3830 (2003).
9. S. E. Offermann, N. H. van Dijk, J. Sietsma, S. Grigull, E. M. Lauridsen, L. Margulies, H. F. Poulsen, M. Th. Rekveldt, and S. van der Zwaag, “Grain nucleation and growth during phase transformations,” *Science* **298**, 1003–1005 (2002).
10. E. M. Lauridsen, H. F. Poulsen, S. F. Nielsen, and D. Juul Jensen, “Recrystallization kinetics of individual bulk grains in 90% cold-rolled aluminium,” *Acta Mater.* **51**, 4423–4435 (2003).
11. S. Schmidt, S. F. Nielsen, C. Gundlach, L. Margulies, X. Huang, and D. Juul Jensen, “Watching the growth of bulk nuclei during recrystallization of deformed metals,” *Science* **305**, 229–232 (2004).
12. H. F. Poulsen and S. Schmidt, “Reconstruction of grain boundaries in polycrystals by filtered back-projection of diffraction spots,” *J. Appl. Crystallogr.* **36**, 319–325 (2003).
13. T. Markussen, X. Fu, L. Margulies, E. M. Lauridsen, S. F. Nielsen, S. Schmidt, and H. F. Poulsen, “An algebraic algorithm for generation of three-dimensional grain maps based on diffraction with a wide beam of hard x-rays,” *J. Appl. Crystallogr.* **37**, 96–102 (2004).
14. G. T. Herman, *Image Reconstructions from Projections. The Fundamentals of Computerized Tomography*, Academic Press, New York (1980).
15. A. C. Kak and M. Slaney, *Principles of Computerized Tomographic Imaging*, IEEE Press, New York (1988).
16. S. R. Deans, *The Radon Transform and Some of Its Applications*, Wiley, New York (1983).
17. R. N. Bracewell and A. C. Riddle, “Inversion of fan-beam scans in radio astronomy,” *Astrophys. J.* **150**, 427–434 (1967).
18. R. Gordon, R. Bender, and G. T. Herman, “Algebraic reconstruction techniques (ART) for three-dimensional electron microscopy and x-ray photography,” *J. Theor. Biol.* **29**, 471–481 (1970).
19. H. F. Poulsen, “A six-dimensional approach to microtexture analysis,” *Philos. Mag.* **83**, 2761–2778 (2003).
20. R. M. Lewitt, “Multidimensional digital image representations using generalized Kaiser-Bessel window functions,” *J. Opt. Soc. Am. A* **7**, 1834–1846 (1990).
21. P. P. B. Eggermont, G. T. Herman, and A. Lent, “Iterative algorithms for large partitioned linear systems, with applications to image reconstruction,” *Linear Algebr. Appl.* **40**, 37–67 (1981).
22. J. Als-Nielsen and D. McMorrow, *Elements of Modern X-Ray Physics*, Wiley, Chichester, England (2001).
23. S. Kaczmarz, “Angenäherte Auflösung von Systemen linearer Gleichungen,” *Bull. Int. Acad. Pol. Sci. Lett., Cl. Sci. Math. Nat., Ser. A* **35**, 355–357 (1937).
24. K. Tanabe, “Projection method for solving a singular system of linear equations and its applications,” *Numer. Math.* **17**, 203–214 (1971).
25. S. Matej and R. M. Lewitt, “Efficient 3D grids for image reconstruction using spherically-symmetric volume elements,” *IEEE Trans. Nucl. Sci.* **42**, 1361–1370 (1995).
26. R. Marabini, G. T. Herman, and J.-M. Carazo, “3D reconstruction in electron microscopy using ART with smooth spherically symmetric volume elements (blobs),” *Ultramicroscopy* **72**, 53–65 (1998).
27. S. Matej, G. T. Herman, T. K. Narayan, S. S. Furuie, R. M. Lewitt, and P. Kinahan, “Evaluation of task-oriented performance of several fully 3D PET reconstruction algorithms,” *Phys. Med. Biol.* **39**, 355–367 (1994).
28. E. Garduño and G. T. Herman, “Optimization of basis functions for

- both reconstruction and visualization,” *Electr. Notes Theor. Comput. Sci.* **46** (2001).
29. A. P. Hammersley, S. O. Svensson, M. Hanfland, A. N. Fitch, and D. Häusermann, “Two-dimensional detector software: from real detector to idealised image or two-theta scan,” *High Press. Res.* **14**, 235–248 (1996).
 30. G. T. Herman, J. Zheng, and C. A. Bucholtz, “Shape-based interpolation,” *IEEE Comput. Graphics Appl.* **12**, 69–79 (1992).
 31. X. Fu, H. F. Poulsen, S. Schmidt, S. F. Nielsen, E. M. Lauridsen, and D. Juul Jensen, “Non-destructive mapping of grains in three dimensions,” *Scr. Mater.* **49**, 1093–1096 (2003).

Xiaowei Fu received his PhD degree in materials science in 1999 from the University of Science and Technology, Beijing, China. After nearly two years at the university as a research and teaching fellow, he moved to the Materials Research Department at Risø National Laboratory, Denmark, as a postdoctoral scientist, where he worked with Prof. Henning F. Poulsen on developing the 3DXRD technique. He is currently a research associate at the Department of Materials Science and Metallurgy, University of Cambridge, UK. His scientific interests are computer modeling, materials characterization, and development of x-ray tomography technique and its application in materials science.

Erik Knudsen: biography and photograph not available.

Henning F. Poulsen is a research professor in the Materials Research Department at Risø National Laboratory in Roskilde, Denmark. His current research interests are in the development of diffraction and imaging techniques based on high-energy x rays and their application to a broad range of topics with relation to polycrystalline materials, and within materials science and engineering in particular areas such as plastic deformation and nucleation and growth phenomena. Poulsen earned his PhD degree in physics from the University of Copenhagen, Denmark, in 1991. Before joining Risø, he spent three years as a postdoctoral researcher at the HASYLAB synchrotron facility in Hamburg, Germany. He has authored or co-authored more than 100 publications, including one book.

Gabor T. Herman is a pioneer in the field of x-ray computerized tomography and is the author of several books and over 100 articles, including many classic works in the field. He is recognized internationally for his major contributions to image processing and its biomedical applications. His PhD is in mathematics. He was the leader of successful image processing groups at SUNY Buffalo and at the University of Pennsylvania, and has garnered millions of dollars in research funding. He is a highly accomplished scientist of international distinction and has been awarded honorary degrees from the universities of Haifa in Israel, Szeged in Hungary, and Linköping in Sweden. He is currently a distinguished professor of computer science at The Graduate Center of the City University of New York.

Bruno M. Carvalho received a BSc degree in computer science from the Federal University of Rio Grande do Norte (UFRN), Brazil, in 1992, and an MSc degree in computer science from the Federal University of Pernambuco (UFPE), Brazil, in 1995. In 1999 and 2003, he received MSc and PhD degrees in computer science from the University of Pennsylvania. He is currently a professor with the Departamento de Informática e Matemática Aplicada, UFRN. His research interests include image reconstruction, image processing, and computer graphics.

Hstau Y. Liao received a degree of nuclear engineer from the Balseiro Institute, National University of Cuyo, Argentina, in 1998, an MSE degree in electrical engineering from the University of Pennsylvania in 2000, and a PhD degree in computer science from the City University of New York in 2005. He is currently a postdoctoral associate at the Institute for Mathematics and Its Applications, University of Minnesota. His research interests include image reconstruction, probabilistic image modeling, and optimization. Liao was awarded bronze and silver medals from the 32nd and 33rd International Mathematical Olympiads and the 5th and 6th Iberian-American Mathematical Olympiads.